

Mechanical Behavior of Steel and Aluminum Foams at High Temperatures

M. Tavares^a, J. M. Weigand^b, L. C. M. Vieira Jr.^a, S. J. C. Almeida^a, S. Szyniszewski^{c,*}

^a*Department of Structural Engineering, State University of Campinas, Campinas, Brazil*

^b*National Institute of Standards and Technology (NIST), Gaithersburg, Maryland, USA*

^c*Department of Engineering, Durham University, Durham, UK*

Abstract

The objective of this study is to quantify and understand the thermo-mechanical behavior of hollow sphere (HS) steel and powder metallurgy (PM) aluminum foams over a broad range of elevated temperatures. The mechanical properties of both the HS steel and PM aluminum foam are measured under compressive loading at ambient (24°C) and temperatures of 100°C , 150°C , 200°C , 300°C , 400°C , 550°C and 700°C , and results for the two foams are compared in terms of their rates of degradation in mechanical properties. The experimental work is underpinned by a computational micro-model, consisting of an assembly of hollow spheres, to link the cell geometry and base metal properties with the global mechanical performance. The computational model shows that plastic buckling of cells with progressive plasticity of the contact area is the key local failure mechanism. As expected due to the plastic buckling of the unit cells, thermal degradations of the tested metallic foams generally follow the same trends as does the yield stress of their bulk metals. The HS steel foam exhibits only minor elevated-temperature-induced degradation in its mechanical properties at or below 400°C , while still maintaining 69 % of its capacity at 550°C . Comparatively, the PM aluminum foam begins degrading at an elevated temperature of only 150°C . Interestingly, the HS steel foam oxidized between

*Corresponding author

Email address: s.szyniszewski@gmail.com (S. Szyniszewski)

300 °C and 400 °C, resulting in increases in the quasi-elastic modulus at elevated temperatures. Future work could explore how to design and take advantage of oxidation reactions at the surfaces of the cells because they could increase mechanical properties of metallic foams at high temperatures. Our computational study also revealed a possibility for a new range of ultra-thin-walled cellular structures, which are predicted to fall within the elastic buckling regime at the local level. Thus, their deformations will be reversible even under high strains and their thermal behavior controlled by the thermal deterioration of elastic constants, and not plasticity parameters such as yield stress.

Keywords: Metallic foam, Plastic buckling, Thermal analysis, Hollow-sphere steel foam, Thermo-mechanical analysis, Fire.

1. Introduction

Cellular materials are commonly found in nature (for example, bird bones and cork) because they are lightweight, and tissue can grow into their open cells enhancing biological interfaces. Metallic foam is an intentionally porous metal substratum largely made up of voids varying in size from nanometers to millimeters. Because the physical parameters of a metal foam, such as its porosity, can be readily controlled during manufacture, the metallic foam's Young's modulus and yield stress can be tuned to satisfy the specific needs, especially in the context of multi-functional and multi-physical engineering applications.

Metallic foams have inherent fire retardancy, low thermal conductivity (relative to traditional steel structural components), and acoustic shielding. Open cell foams, albeit more expensive than traditional materials, also provide air, vapor, and fluid transport capabilities. Open cell foams act efficiently as heat exchangers due to the turbulent well-mixing flow that occurs within the foam's irregular micro-structural cavities, combined with the large surface area of their pores and the high thermal conductivity of their base metals. The influences of various micro-structural properties of metal foams, such as their porosity,

pore and fiber diameters, tortuosity, pore density, and relative density on the heat exchanger performance were discussed in [1]. Vadwala et al. [2] showed
20 that a new composite material combining copper foam with wax was efficient in increasing the thermal conductivity of thermal energy storage systems. Cellular metals are also used as catalyst support in fuel cells. Their large surface area and mixing potential increases the intensity of the interaction between the catalyst and the fluid medium. Yuan et al. [3] provides a review of the fabrication,
25 characterization, and application of porous metal materials for application to fuel cells.

While existing applications for metallic foams reside largely in the mechanical, aerospace, and automotive domains [4], decreasing manufacturing costs and more widespread adoption of full-scale production techniques has ushered in the
30 potential for using metallic foams in civil infrastructure applications. Metallic foams exhibit excellent stiffness-to-weight ratios, in comparison to traditional building materials, under a variety of loading conditions. For example, Banhart and Seeliger [5] showed that foam panels have higher bending stiffness than solid steel sheets of the same weight. Metallic foams are also renowned for their
35 compressibility because they can reliably sustain 90 % engineering strain prior to failure [6], lending them extraordinary energy dissipation capacity [7]. Energy dissipation via large compressive deformations at low-amplitude constant stress levels has been explored by the automotive industry as a potential crash protection technology [8].

40 The ambient-temperature mechanical properties of metallic foams – particularly steel and aluminum foams – are characteristically different from those of their solid base metals. Steel foam is highly-compressible after yielding, unlike solid steel [9], which exhibits only shear deformations and is incompressible in the plastic regime. Also, foams often fracture under tensile strains that are
45 noticeably lower than their crushing and compaction strains [10] thus warranting tailored respective failure criterions. Szyniszewski et al. [11] tested steel foam to measure its compressive yield stress, densification strain, compressive plastic Poisson's ratio, compressive unloading modulus, as well as axial and

shear mechanical properties at ambient temperature. [11] noted the importance
50 of correctly assessing Poisson's ratio due to its link to foam compressibility as
shown by Deshpande and Fleck [9].

Elevated temperatures have a significant influence on the compressive behavior of metallic foams. Aly [12] tested closed cell aluminum foams under compressive loads at temperatures ranging from 25 °C to 620 °C, and concluded that the compressive strength decreases both as the foam's density decreases and when temperature increases. Kovavcik et al. [13] studied the high-temperature (20 °C to 500 °C) compressive behavior of powder metallurgy aluminum foams. They observed that increased temperatures resulted in decreased compressive strength, decreased energy absorption capacity, and increased densification strain (plateau length) at constant density. Kovavci et al. [13] also reported that exposure time (of the elevated temperatures) did not influence the compression behavior of foams. Liu et al. [14] investigated Al-Si-SiC composite foams under compression at elevated temperatures, evaluating the influence of temperature on energy absorption and type of fracture. Liu [14] reported a decrease in compressive strength with increasing temperature, as well as a decrease in the absorbed energy where ductile-type fracture mode occurred. Taherisharg et al. [15] analyzed expanded perlite-aluminum syntactic foam at elevated temperatures and compared the results with those of the matrix materials, tested under the same conditions. Their results indicated that the high-temperature mechanical properties of the foams are controlled both by softening of the matrix materials and the improved ductility of the foam. Bekoz and Oktay [16] tested the mechanical properties of powder metallurgy steel foams at ambient and elevated temperatures, and reported an increase in compressive yield strength and stiffness for temperatures at or below 400 °C, and a decrease in compressive yield strength and stiffness above that temperature. They [16] concluded that the aging effect (i.e., dynamic age-hardening) was responsible for the increase in mechanical properties up to 400 °C. As a continuation of the work presented in Szymiszewski et al. [11], this study examines the thermo-mechanical behavior of hollow-sphere (HS) steel foam samples removed from the same rectangular

80 prism. Specifically, this paper characterizes and compares the mechanical properties of HS steel and powder-metallurgy (PM) aluminum foam specimens at elevated temperatures. Both the steel and aluminum foams are exposed to a wide range of elevated temperatures, up to 700 °C and 500 °C, respectively, for durations of 15 min and 30 min.

85 **2. Experimental approach**

Material samples

A HS steel foam rectangular prism, sourced from Fraunhofer Institute (Germany), with dimensions 22 cm × 5.2 cm × 5.2 cm, was cut and machined into 10 cylindrical specimens following the specifications in the ISO Standard
90 13314:2011 [17]. The cylindrical specimens had a diameter of 25 mm and length of 50 mm (Figure 1).

According to ISO standard for testing, all spatial dimensions of the specimen shall be at least 10 times larger than the average pore size and no less than 10 mm, and the ratio of the length to the diameter shall be between 1.0 and 2.0.
95 The measured average pore size was 2.27 mm as explained below. Between 12 and 14 spheres typically spanned across the 25 mm radius. The specimens had an average 85 % porosity, calculated based on the dimensions and volume of the specimens. The base metal was mild steel with 0.3 % - 0.5 % carbon content and 0.5 % phosphorous content. Based on that chemical composition,
100 the base metal's bulk yield stress was estimated as 250 MPa, using the method outlined in [18]. [19] a reported a yield stress of 260 MPa for the same material. The ultimate tensile capacity of the base metals was estimated as 500 MPa, based on tests performed by IFAM on tensile specimens produced by Spark Plasma Sintering and homogenization annealing. This estimate was consistent
105 with data for alloys with similar carbon and phosphorous contents reported in the literature, see Worldwide Guide to Equivalent Irons and Steels – table with Australian steel [18].

The PM aluminum foam had dimensions $14.8\text{ cm} \times 6.0\text{ cm} \times 6.0\text{ cm}$ and was sourced from Fraunhofer Institute for Machine Tools and Forming Technology IWU, Chemnitz, Germany. Like for the HS steel specimens, the PM aluminum foam rectangular prism was machined into 8 cylindrical specimens, each with a diameter of 25 mm and length of 50 mm, in accordance with ISO 13314:2011. Due to the inherent heterogeneity of PM foams, the porosity varied between 71.4 % and 81.8 % for the 8 cylindrical specimens. The base metal consisted of a common aluminum alloy AW-6060 (AlMgSi0.5).

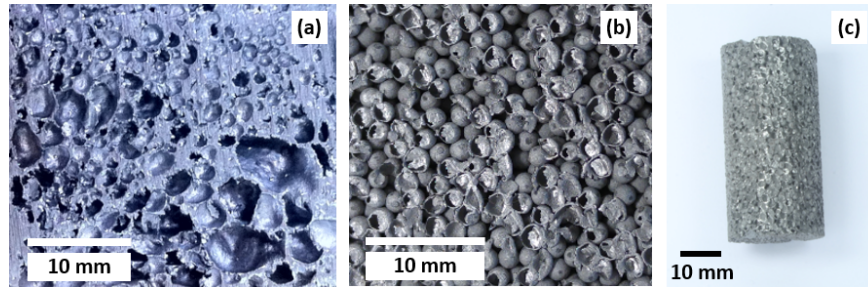


Figure 1: Metallic foam samples: (a) aluminum, (b) hollow sphere steel and (c) actual steel specimen before testing. Metallic foams are cellular metals, where steel foam resembles closely packed hollow spheres.

Pore Size Dimensions

The pore size dimensions were determined to ensure that each cross-section contained a sufficient number of pores to achieve homogeneous material properties. Based on a high-definition image of a transversal cut of the base samples, the largest dimension of 242 pores for HS steel foams and 237 pores for aluminum foam were measured. The 20 mm distance between the jaws of a Mitsuo digital caliper was used as a reference length for the pixel distance measurement. 726.20 pixels = 20 mm in the HS steel foam, and 236.51 pixels = 10 mm in the PM aluminum foam (see Figure 2).

Normal distribution function with mean equal to 1.79 mm and variance of 0.19 mm^2 best described the pore size measurement in HS steel foam (Figure

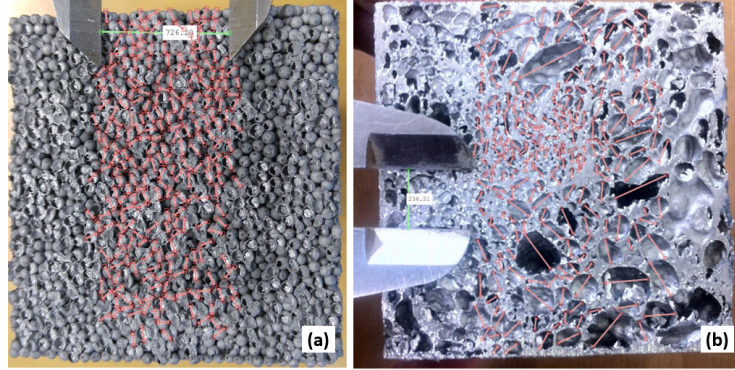


Figure 2: Measurement of the pore size: (a) HS steel foam and (b) aluminum foam sample. Diameter of the spherical shell affects its stability and load capacity.

3a). On the other hand, aluminum foam pore size was best described by a lognormal function with mean equal to 2.13 mm and variance equal to 1.67 mm² (Figure 3b).

130 If the pore shape is spherical, the measurement of the pore size through a transversal cut will be smaller than the pore diameter, unless the cut passes exactly through the pore center (Figure 4). Thus, an amplification factor was proposed to improve the estimate of the pore diameter from sectional pore measurements.

135 Let us consider an unknown amplification factor as the ratio between the mean of the projected radius values and the true sphere's radius (Figure 5). If one assumes that all pores are spherical, random cuts can be generated using a uniform random distribution of $h_{proj} \in \langle 0, r_{true} \rangle$ and for each cut a projected radius can be computed as:

$$r_{proj}^i = \sqrt{r_{true}^2 - h_{proj}^i} \quad (1)$$

140

Employing Monte-Carlo simulation, we computed the average value of \hat{r}_{proj}

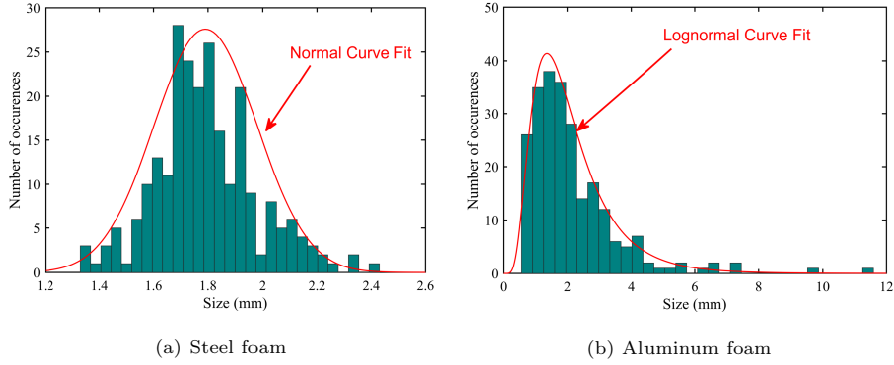


Figure 3: (a) Normal distribution of pore size – HS steel foam, (b) Lognormal distribution of pore size – aluminum foam. Hollow sphere foam exhibits lower variability than powder metallurgy foam, characterized by larger scatter of pore sizes.

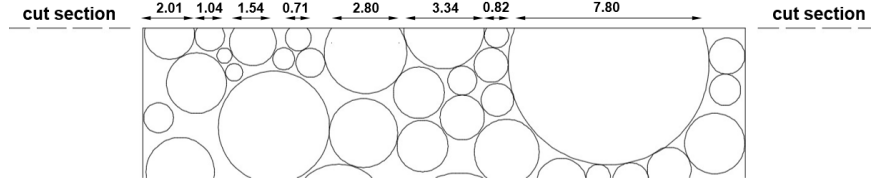


Figure 4: Schematic lateral view of the cut plane on the sample. One can notice that cross-sectional diameters do not coincide with the true diameter of the sphere or cavity.

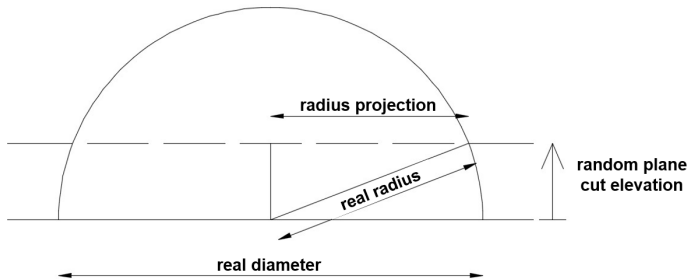


Figure 5: Cutting a sphere at random elevations we computed the relationship between the expected mean radius in the cut plane and the real radius of the spherical cavity.

and consequently computed the correction factor as:

$$\alpha = \frac{r_{true}}{\hat{r}_{proj}} \quad (2)$$

An amplification factor $\alpha = 1.27$ was obtained resulting in corrected pore diameter of $1.27 \times 1.79 = 2.27$ mm in HS steel foam and $1.27 \times 2.13 = 2.70$ mm for aluminum foam, which leads us to conclude that the specimens must have at least 22 mm and 27 mm of cross-sectional width respectively. Considering the size of aluminum and steel foam blocks, 25 mm diameter was chosen for both base materials.

3. Behavior of HS steel and PM aluminum metallic foams at elevated temperatures

Mechanical testing

Steel foam specimens were tested at 24 °C (ambient temperature), 150 °C, 200 °C, 300 °C, 400 °C, 550 °C, and 700 °C, while aluminum foam specimens were tested at 24 °C, 150 °C, 200 °C, 300 °C, and 500 °C (Table 1). For the most part, two specimens were tested at each temperature except ambient; one exposed to the elevated test temperature for 15 min, and the other exposed for 30 min. The exceptions were the 550 °C and 700 °C tests on the HS steel foam, and the 500 °C test on aluminum foam, which were all exposed for only 15 min. For each test, the high-temperature furnace was heated to the test temperature without the specimen inside. Once the targeted elevated temperature was reached, the cylindrical metallic foam specimen was placed inside the furnace. The compressive test was not started until the specimen had reached and been held under a steady-state conditions at the target testing temperature for the required exposure time. The testing temperature was regulated by a thermocouple installed on the side of each specimen. [20] reported that mild steel melts at a temperature of approximately 1536 °C, and [7] estimated the aluminum melting temperature at approximately 660 °C. The majority of the

testing temperatures was conducted at elevated temperatures less than 400 °C
¹⁷⁰ because, based on both the available literature and EN 1993-1-2:2005 [21], the strength of steel is severely degraded at elevated temperatures exceeding 400 °C. The sensitivity of the mechanical properties to exposure time was evaluated by conducting the compressive testing following both 15 min and 30 min of steady-state pre-heating.

Table 1: Temperature and exposure time during compressive experiments

Temperature		Steel Foam		Aluminum Foam	
(°C)	Melting point (%)	Duration (min)	Melting point (%)	Duration (min)	
24	2	∞	4	∞	
150	10	15 & 30	23	15 & 30	
200	13	15 & 30	30	15 & 30	
300	20	15 & 30	45	15 & 30	
400	27	15 & 30	-	-	
500	-	-	76	15	
550	37	15	-	-	
700	47	15	-	-	

¹⁷⁵ *3.1. Testing approach*

The compressive testing was conducted using a servo-hydraulic Materials Testing Systems (MTS) Model 810 Universal Testing Machine (UTM), with a capacity of 100 kN in compression, and an MTS Model 652.01 High-Temperature Electric Furnace applied the thermal loads (Figure 6).

¹⁸⁰ Mechanical loads in the UTM were controlled using a MTS Flex Test 60 controller, and the furnace was controlled using a MTS Digital PID Temperature Controller. The high-temperature furnace allows pre-heating at temperatures up to 1000 °C, has multi-zone temperature control to compensate for vertical temperature gradients, and is accurate (at the constant steady-state temperature) to within ± 2 °C. After a preload of 0.10 kN was applied to remove
¹⁸⁵

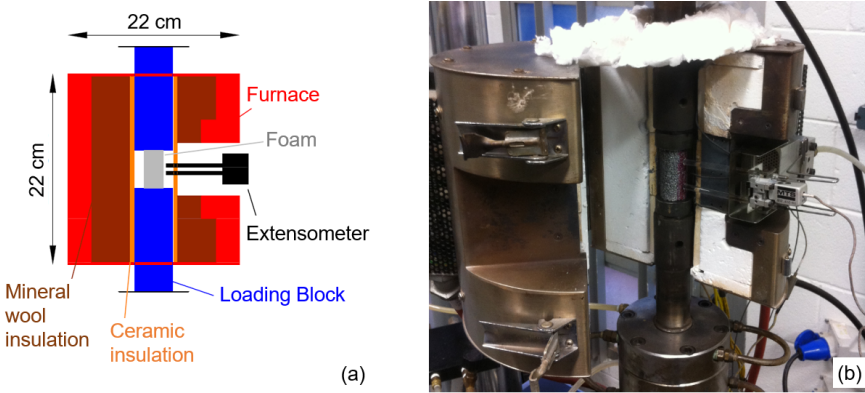


Figure 6: Thermal-mechanical compressive test setup: (a) annotated schematic of high-temperature furnace, and (b) Actual view of the opened furnace. Sample is heated first, and loaded after stable internal temperature is reached. Strains were measured with an extensometer inside the furnace.

any surface irregularities, axial loading was applied pseudo-statically using displacement control at a constant loading rate of 0.025 mm/s. The reported compressive stress, σ , was calculated as the ratio of the applied force F to the measured cross-sectional area before loading. Ideally, the reported compressive strain ϵ would be measured using the available MTS High-Temperature Axial Extensometer. However, for many specimens the tips of the extensometer leads slipped at relatively low compressive loads, and thus for consistency the compressive strain was calculated as the ratio of crosshead displacement to the measured length of each undeformed cylindrical specimen.

195 3.2. Experimental stress-strain curves

The compressive stress-strain behavior of metallic foams exhibited three distinct phases of behavior (Figure 7). Until yield, the behavior was elastic (Elastic Phase), and the stress was linearly related to the strain. After yield was a large plastic plateau (Plateau Phase). Within this region, an upper and lower yield point can be identified. The final phase (Densification Phase) is characterized by densification of the metallic foam, during which the stiffness of the compres-

sive stress-strain curve rapidly increases. During densification, the cell walls of the metallic foam begin to buckle and contact one another as the voids close. The densification phase continues until the metallic foam reaches its compressibility limit. The slope of the stress-strain curve within the densification phase 205 is defined as the densification modulus.

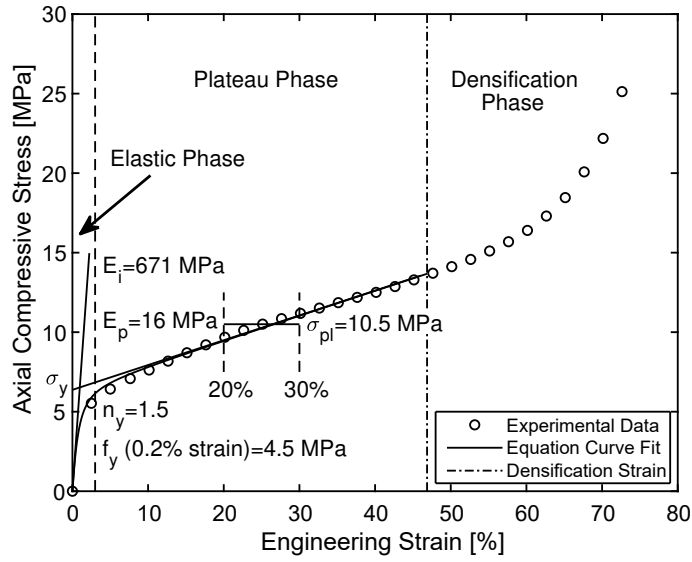


Figure 7: Parametrization of a typical, non-linear stress strain curve of metallic foam. Initial modulus corresponds to the foam stiffness, yield stress is computed at 0.2% offset, plastic hardening is the linear fit and plateau stress is the average stress in the range of 20-30% strains. Curvature of the transition from elastic to plastic behavior is characterized with parameter n_y .

Results from the steel and aluminum foam specimens tested under uniaxial compression at elevated temperatures are shown in Figures 8a) and 8b), respectively. Similar trends were observed for both types of metallic foam, in that each specimen exhibited, but to varying degrees, the three phases of behavior 210 shown in Figure 7. The exposure (15 min or 30 min) did not appear to have had a systematic influence on the stress-strain behavior of the specimens.

An insightful reader can notice that properties at 300C are higher than room temperature or 100C. In addition, those from 400C are higher than those from

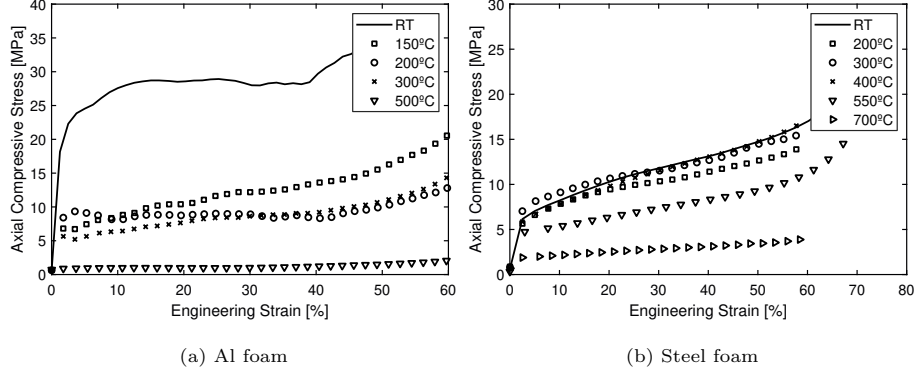


Figure 8: Stress-strain behavior of metallic foam samples as the ambient temperatures increases. Whereas Al foam loses 50% of its capacity at 150 °C only, Fe based cellular structure maintains its strength up to 400 °C.

215 200C, which seems puzzling at first. However, we observed a thin, blue oxide film on all cells of steel foam at temperatures exceeding 250C (see Figure 9). The effect of steel oxidation at around 300C, the so-called “blue brittleness effect”, is a phenomenon that occurs in steel alloys with significant Carbon content upon heating; particularly within temperatures ranging of 180 °C to 370 °C ([22]).
 220 The blue oxide layer, which forms on the surface of the metal, is stiffer and stronger than the base steel alloy but more brittle. The addition of a stiffer film on the cells increase the macroscopic stiffness of the foam due to the large surface area relatively to the volume of the base material. The effect of the distributed stiffening of the steel foam become negligible at higher temperatures ad the base
 225 steel of the cells loses its stiffness and strength.

The effect of a blue oxide film was also observed in the systematic analysis of the macroscopic steel foam properties at elevated temperatures described later in the paper.



Figure 9: (left) HS steel foam specimen before testing, (right) HS steel foam specimen after testing at 300 °C following 30 minute exposure. Discoloration of the heated specimen indicated formation of the blue oxide film, which was highly likely stiffening the spherical shells. Formation of the stiffer oxide layer could explain better experimental performance of the steel foam samples, in comparison to the simulated predictions.

4. Micro-mechanical simulations

The microstructure of a sintered HS foam consists of the hollow spheres and the welds between those spheres. The spheres have been shown to be in a random close-packed (RCP) stacking [23]. [24] tested five algorithms for the generation of random RCP sphere stacking and showed that two different variations of the “Mechanical Contraction Method” resulted in RCP stackings that were most like an experimental stacking in their geometric properties. The algorithmically simpler of those two methods, the “Modified Mechanical Contraction Method”, was chosen for the presented simulations, which involves the steps below ([25], [26]):

1. Randomly place spheres of zero size throughout the domain.
2. Increase the size of all spheres by an equal magnitude.
3. Check for overlapping spheres and move both spheres in each overlap pair away from each other by an equal magnitude. Repeat this step until all

but a minimum threshold of overlaps are eliminated.

4. Repeat steps 2 and 3 until the final sphere size is reached.

After the spheres are successfully placed, the welds are inserted to connect them. The actual welds between the spheres are solid circular shapes with concave sides which curve until they reach a tangent with the sphere. However, due to the difficulty of modeling such a shape, these welds were approximated by a straight cylinder of a given diameter connecting any spheres that are within a specified threshold distance of each other. The random variables in this geometry algorithm include the sphere size, wall thickness, and sphere location. The deterministic variables include the weld size, structure, and some of the input parameters for the Modified Mechanical Contraction Method such as the number of spheres to initially place and the number of overlaps threshold at which to increment the size of the spheres. Detailed description of the micro-simulator can be found in [19]. The algorithm produced geometries such as that displayed in Figure 10a). The generated geometry was then used as the mesh to create a finite element model in the LS-DYNA software package, with mechanical properties of the base steel at ambient temperature and 550 °C as shown in Table 2.

Table 2: Mechanical properties employed in the simulations.

Property	Value	
	Ambient	550 °C
Young modulus	200 GPa	91 GPa
Poisson ratio	0.29	0.29
Yield stress	250 MPa	67.5 MPa
Ultimate strain	0.18	0.21
Ultimate strength	600 MPa	192 MPa

Von Mises effective stress of the model under increasing compressive pressure (Figure 10b-c) indicated localized plasticity at the sphere interfaces, which

led to sphere deformations. Simulated stress strain curve compared well with the experimental curve (see Figure 10d). The simulated curves became irregular at large strains because the implicit algorithm used in LS-DYNA struggled to converge on account of the large number of contact surfaces. The simulated curve at 550 °C is noticeably higher than the experimental curve. This discrepancy is attributed to strengthening of the spherical shells due to oxidation of the steel foam at elevated temperatures (see Figure 9). This strengthening was not accounted for in the computational model.

The plastic strains localized in a few contact locations at 1.2% global engineering strain with progressively more localized plasticity regions with larger volume appearing at larger strains (Figure 11a-c). Cross-sections of the micro-model in Figure 11d-f illustrate the typical deformation mechanism. One should be aware the spheres are axi-symmetric. The key parameters identified by [27] such as sphere radius, R , its thickness, t , material properties of the base material and the diameter of the contact area are significant. The simulations showed that the diameter of the contact area was not constant; it gradually increased until the sphere collapsed at large strains. The simulations clearly indicated that plasticity dominated the local deformations.

4.1. Insights from the analytical expressions for buckling of a spherical shell

Pressure applied to a sphere, q_c needs to satisfy equilibrium with the membrane stress within the walls of the spherical shell:

$$\sigma_{shell} 2\pi R t = q_c \pi \frac{d_c^2}{4} \quad (3)$$

Thus, the membrane stress resulting from the applied pressure can be approximated as:

$$\sigma_{shell} = q_c \frac{d_c^2}{8Rt} \quad (4)$$

When the critical limit of the membrane stress is exceeded, it may fail either due to material yielding at the elastic limit, σ_y or due to the buckling arising

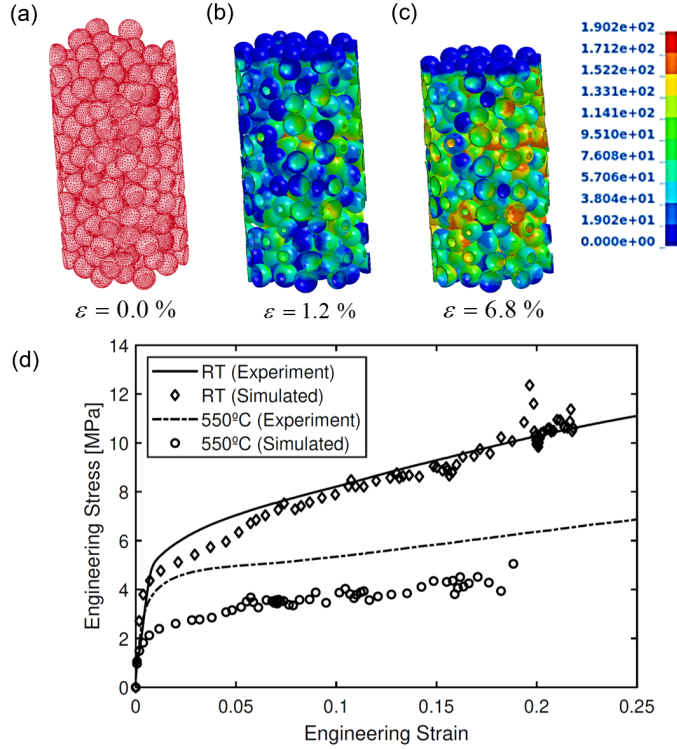


Figure 10: Comparison of experimental (diamonds and circles) and computational (continuous lines) strength predictions at room (RT) and high temperature (550°C). Von Mises stress (MPa) localized in the contact regions of the hollow steel spheres. Multiple and irregular load paths followed the random packing of the spheres, which resulted from the nature of the manufacturing process. Whereas simulated and experimental data showed good agreement, steel foam samples exhibited higher stiffness and strength at high temperatures when compared to the computational prediction.

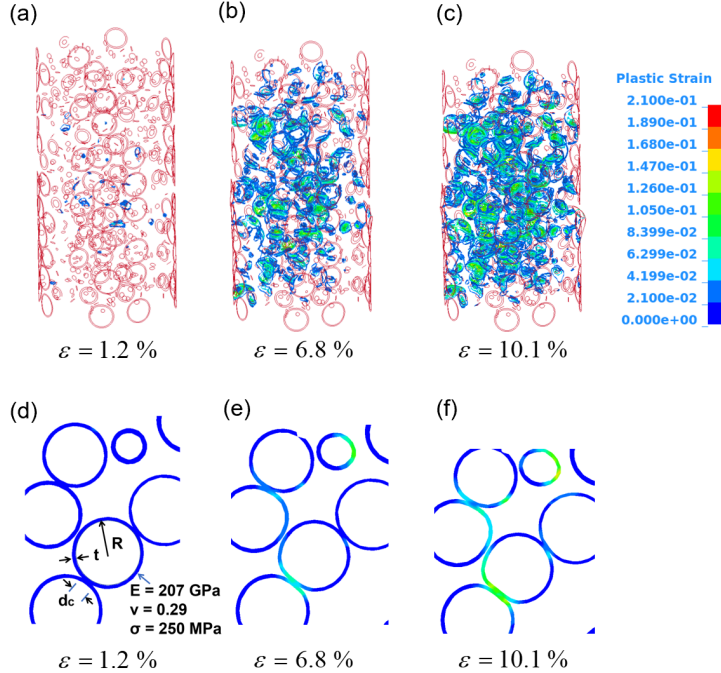


Figure 11: Plasticity localized at sphere interfaces experiencing plastic deformations arising from contact forces. As the load increased, the number of contact pairs and subsequently, plastic regions surged (b-c). Radius, R and thickness, t of the spherical shell, the diameter of the contact interface, d_c and material properties of the hollow spheres influence the local resistance mechanism (d). Following the initial yielding around the contact region, the plasticity spreads toward the equator of the sphere, accompanied by the gradually increasing diameter of the plastic hinge hoop moving outwards from the initial contact area (e-f). Due to the random packing, the number of contact regions and their directions vary from sphere to sphere, which is consistent with experimental study reported by Fallet et al. in [27].

from its geometric imperfections. Shell stress limit to avoid the elastic buckling
290 is after [28]:

$$\sigma_{cr} = \frac{Et}{R\sqrt{3(1-\nu^2)}} \quad (5)$$

Material yielding typically leads to geometrical buckling anyway and the loss
of the ideal spherical shape. Thus, the shell capacity of a hollow sphere can be
expressed as:

$$\sigma_{failure} = \min(\sigma_y, \sigma_{cr}) \quad (6)$$

295

In the simulations, the steel base metal had Young modulus $E = 200$ GPa,
Poisson ratio $\nu = 0.29$, and yield stress $\sigma_y = 250$ MPa. The average radius of
the spheres and thickness were reported in a previous study [11] as $R = 1.86$ mm
and $t = 0.02$ mm. The resulting geometrical slenderness, expressed as a radius
300 to thickness ratio such that $R/t = 93$, is consistent with the plastic buckling
region (Figure 12a). A more general measure of the slenderness is the ratio
of the plastic yield stress to the elastic buckling stress because it includes the
effects of the material properties on the slenderness:

$$\lambda = \frac{\sigma_y}{\sigma_{cr}} \quad (7)$$

305 If slenderness $\lambda < 1$, then the structure is controlled by the material fail-
ure, namely plastic yielding. Alternatively, $\lambda > 1$ indicates high slenderness
and propensity for elastic buckling (Figure 12b). [29] developed an empi-
rical curve for metallic plates, which showed that the transition between plastic
and elastic buckling capacities is more gradual and that there exists additional
310 post-buckling reserve capacity in the elastic buckling regime. Even consider-
ing Winter's curve, the HS steel foam, as well as other foams reported by [27],
are controlled by plastic buckling. Interestingly, elastic buckling equations for

spherical shell also described elastic buckling capacity of a circular shell. Thus,
 the buckling curve in Figure 12b can also be used to analyzed hollow tubular lattice structures.
 Even considering the lightest metallic material achieved
 to-date by [30], only one of their configurations was in the elastic buckling re-
 gion. Schaedler's experiments showed that the slender lattice exhibited large,
 reversible deformations, while the stub lattices experienced non-reversible de-
 formations but higher absolute strength. These experimental observations are
 consistent with plastic and elastic buckling of the cylindrical shells at the junc-
 tions of the hollow tubular struts.

Based on a review of available data, conventionally produced HS foams ex-
 hibit local deformation mechanism controlled by the plastic buckling of the
 spherical shells. Thus, the thermal degradation of the global mechanical prop-
 325
 320
 315
 300
 290
 280
 270
 260
 250
 240
 230
 220
 210
 200
 190
 180
 170
 160
 150
 140
 130
 120
 110
 100
 90
 80
 70
 60
 50
 40
 30
 20
 10
 0

Based on a review of available data, conventionally produced HS foams exhibit local deformation mechanism controlled by the plastic buckling of the spherical shells. Thus, the thermal degradation of the global mechanical properties of our HS foam specimens is anticipated to be controlled by the influence of elevated temperatures on the base metal's yield stress.

Regarding the influence of the temperature on the stiffness of the foam, radial displacement of a spherical shell under uniform external pressure, q is a function of its geometry and elastic constants:

$$w(\varphi) = \frac{q(1 + \nu)R^2}{Et} \left[k(\varphi) \cot \varphi + \cos \varphi - \frac{1}{1 + \cos \varphi} \right] \quad (8)$$

330

where $k(\varphi)$ is the auxiliary variable:

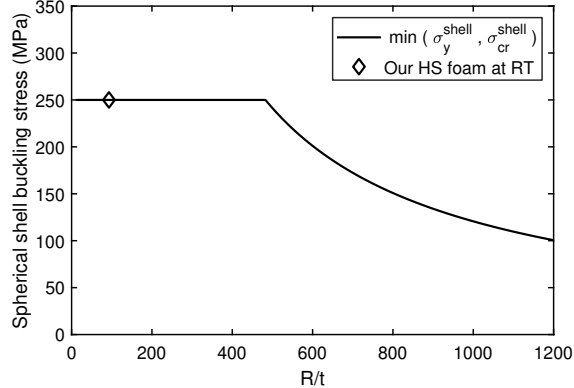
$$k(\varphi) = \left(1 - \frac{1}{1 + \cos \varphi} + \log(1 + \cos \varphi) \right) \sin \varphi \quad (9)$$

The deformation of the apex corresponds to $\varphi = \frac{\pi}{2}$, which gives:

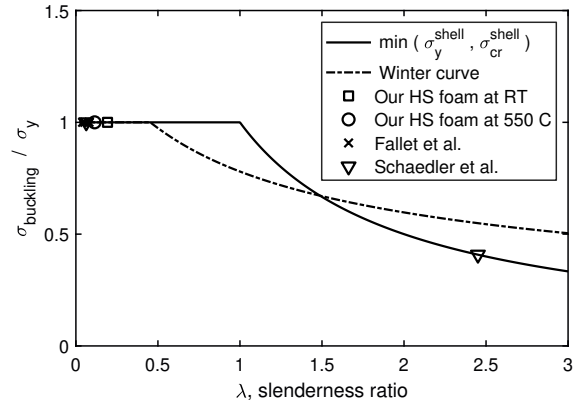
$$w_{apex} = -\frac{q(1 + \nu)R^2}{Et} \quad (10)$$

Since the direct influences of temperature on the radius and thickness of
 335
 325
 315
 300
 290
 280
 270
 260
 250
 240
 230
 220
 210
 200
 190
 180
 170
 160
 150
 140
 130
 120
 110
 100
 90
 80
 70
 60
 50
 40
 30
 20
 10
 0

Since the direct influences of temperature on the radius and thickness of the sphere, as well as Poisson's ratio, are expected to be minimal, the thermal



(a) The effect of geometric slenderness on the buckling capacity of a single sphere.



(b) The effect of slenderness ratio on the buckling strength of a hollow sphere.

Figure 12: Buckling capacity of a single spherical shell expressed in terms of its critical membrane stress. Geometric slenderness of our hollow sphere steel foam expressed as the ratio of radius to thickness, R/t is low and consistent with the plastic buckling mechanism. Normalized theoretical buckling stress as a function of the non-dimensional slenderness parameter, λ overlaid with a range of theoretical capacities of foams and tubular lattice structures. Apart from the ultra-light metallic lattice, most of the manufactured cellular structures have very low slenderness, which is consistent with the irreversible, plastic buckling.

degradation of the foam *stiffness* is anticipated to be controlled by the base metal's Young modulus.

5. Standard Metrics Calculated based on ISO Standard 13314:2011

The following sections synthesize experimental observations to reveal the trends of the macroscopic material properties such as the plateau stress and Young's modulus as a function of the ambient temperature. Based on the computational and analytical considerations described in Section 3, it was anticipated that the phenomenological properties of the HS foam, with stub spherical shells, would primarily reflect the thermal degradation trends of their base metals.

5.1. Yield Strength

Porous metallic materials are known to exhibit substantial plastic yielding capacity following an initial elastic phase, but they do not typically exhibit a "yield plateau". Therefore, ISO Standard 13314:2011 recommends using the 0.2 % strain offset method to calculate the quasi-elastic compressive yield strength of porous metallic materials. Figure 13 show the retained yield strength of the HS steel and PM aluminum foams. At temperatures at or below 400 °C the HS steel foam retained an average of about 80 % of its ambient-temperature yield strength, but at temperatures exceeding 400 °C the yield strength was significantly degraded. The PM aluminum foam retained an average of less than 50 % of its ambient-temperature yield strength at or below 200 °C, and the retained yield strength was only 4.4 % at 500 °C.

5.2. Plateau Stress

The plateau stress, shown in Figure 14, was calculated following ISO Standard 13314:2011 as the average value of the stresses within the strain range spanning from 0.20 mm/mm and 0.30 mm/mm. There was little degradation in the measured plateau stress of the HS steel foam specimens at or below a 400 °C. However, the plateau stress of the PM aluminum foam specimens had

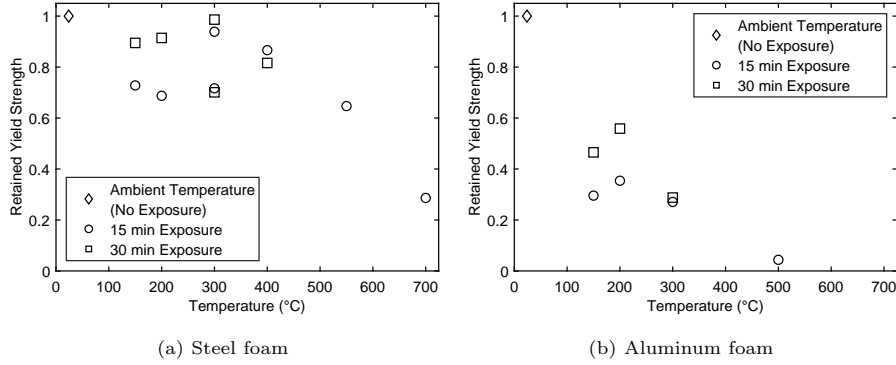


Figure 13: Retained quasi-elastic modulus (i.e., the ratio of the quasi-elastic modulus for a specimen tested at temperature $T > T_{\text{amb}}$ to that of a specimen tested at ambient temperature). The quasi-elastic modulus is the initial slope of the elastic phase of the compressive stress-strain curve. Elastic modulus degrades noticeably at 700 °C for steel foam, and at 150 °C for Al foam

significantly degraded by approximately 50 % at only 150 °C (i.e., at only 23 % of aluminum's melting point).

The exposure (15 min or 30 min) had relatively little influence on the retained plateau stress for the HS steel foam; the retained plateau stress for the two exposures did not differ by more than 4.0 %. The retained plateau stress of the PM aluminum foam was more scattered, but no systematic influence of exposure on the energy absorption capacity was observed. It was observed that the porosity of the PM aluminum foam specimens ranged from 71.4 % to 81.8 %, which may have increased the variability in their calculated mechanical properties, relative to those for the HS steel foam specimens.

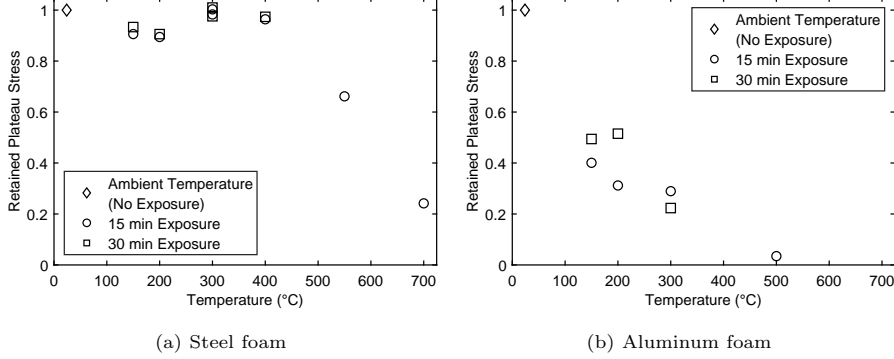


Figure 14: Retained plateau stress (i.e., the average stress in the range of 20-30% engineering strain) of a specimen tested at temperature $T > T_{\text{amb}}$ to that of a specimen tested at ambient temperature. The plateau stress degrades noticeably at 550 °C for steel foam, and at 150 °C for Al foam.

5.3. Additional Metrics Calculated based on Multi-Parameter Curve Fit

To further characterize the response of the HS steel and aluminum foams,
375 the nine-parameter phenomenological equation

$$\sigma(\varepsilon, T) = \begin{cases} \frac{(E_i(T) - E_p(T)\varepsilon)}{\left(1 + \left|\frac{(E_i(T) - E_p(T)\varepsilon)}{\sigma_y(T)}\right|^{n_y(T)}\right)^{\left(\frac{1}{n_y(T)}\right)}} + E_p(T)\varepsilon, & \varepsilon \leq \varepsilon_d \\ \sigma_d + \frac{(E_b(T) - E_d(T))(\varepsilon - \varepsilon_d(T))}{\left(1 + \left|\frac{(E_b(T) - E_d(T))(\varepsilon - \varepsilon_d(T))}{\sigma_p(T)}\right|^{n_b(T)}\right)^{\left(\frac{1}{n_b(T)}\right)}} + E_d(T)(\varepsilon - \varepsilon_d(T)), & \varepsilon > \varepsilon_d \end{cases} \quad (11)$$

where

$$\sigma_d(T) = \frac{(E_i(T) - E_p(T))\varepsilon_d(T)}{\left(1 + \left|\frac{(E_i(T) - E_p(T))\varepsilon_d(T)}{\sigma_p(T)}\right|^{n_y(T)}\right)^{\left(\frac{1}{n_y(T)}\right)}} + E_p(T)\varepsilon_d(T), \quad (12)$$

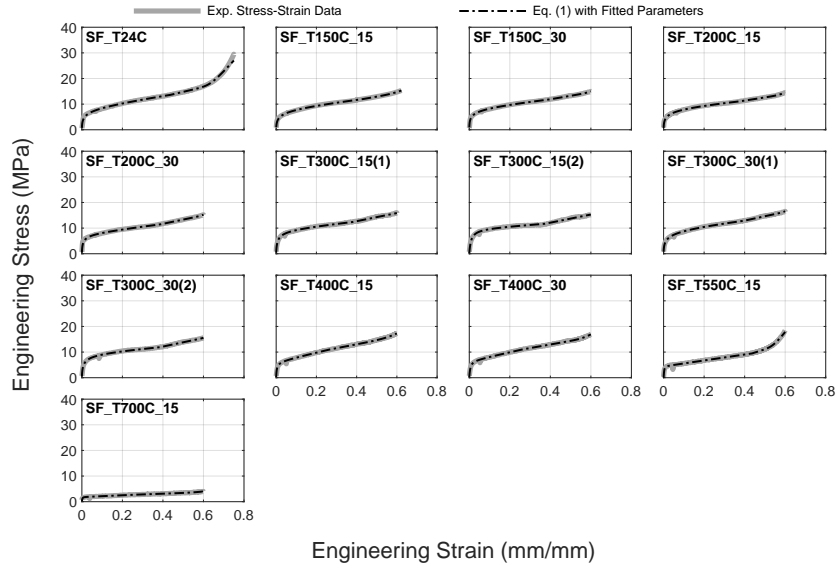
was fitted to the compressive stress-strain response of each specimen. Similar five-parameter models have been successfully used in previous research to

380 characterize the thermal-structural performance of structural components, such
as high-strength bolts (see [31]). Equation 11 is piecewise; each of the two seg-
ments is based on the nonlinear four-parameter “Richard Equation”, which was
formulated by [32]. In Eqs. 11 and 12, σ is the compressive stress, ε is the
compressive strain, E_i and E_p are initial elastic and plastic hardening modulus
385 of the stress-strain response, respectively, σ_y is a reference load that corresponds
to the projection of the plastic modulus at zero strain, n_y is a shape parameter
that controls the sharpness of the transition from the elastic stiffness to the
plastic stiffness, ε_d is the densification strain, $(\varepsilon_d, \sigma_d)$ is the stress-stain coor-
dinates of the inflection point defining the transition to stiffening behavior, σ_p
390 is the projection of the densification stress at zero strain, n_d is a shape param-
eter controlling the sharpness of the transition from the plastic stiffness to the
densification stiffness E_d . (T) denotes dependence of the stiffness or capacity
parameter on temperature.

395 The fitted values for the parameters in Eq. 11 were determined using con-
strained gradient-based nonlinear multivariable optimization techniques avail-
able in MATLAB’s Optimization Toolbox ([33]). Tables 3 and 4 (located in the
appendix) presents a summary of the final fitted parameters for each individual
foam specimen, and quality of the analytical fits is also shown in Figures 15.
400 Discussion on each of the calculated parameters is provided in the following
sections.

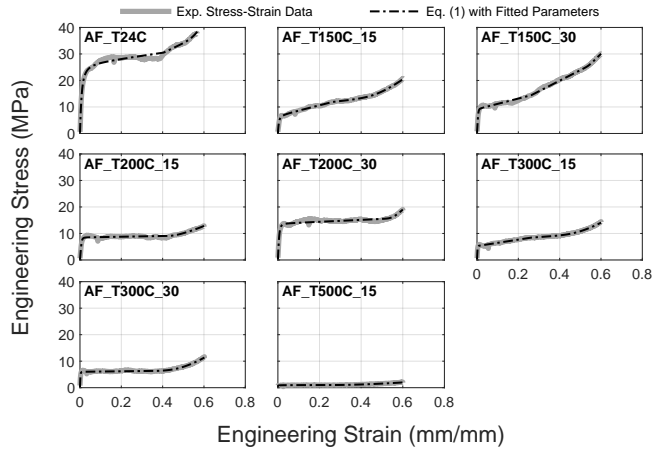
5.3.1. Quasi-Elastic Modulus

405 The quasi-elastic modulus is the initial slope of the elastic phase of the
compressive stress-strain curve. It should be noted that the definition of the
quasi-elastic modulus differs slightly from that of the elastic gradient, which
can be calculated only after the specimen has been loaded and subsequently
unloaded. The quasi-elastic modulus was calculated by fitting Eq. 11 within
[0, ε_y], where ε_y is the yield strain calculated using the 0.2 % offset method
recommended by ISO Standard 13314:2011. Figures 16a and 16b show Eq.
11, with fitted parameters calculated using structural optimization techniques,



Engineering Stress (MPa)

(a) Steel foam



Engineering Stress (MPa)

(b) Aluminum foam

Figure 15: Eq. (9) fitted to the full stress-strain behavior of each specimen for: (a) HS steel foam specimens, and (b) PM aluminum foam specimens. Each plot is denoted by specimen name, using an annotation located in the upper-left-hand corner.

⁴¹⁰ relative to the stress-strain data in the elastic phase. Obviously, Eq. 11 can provide a very close approximation to the actual experimental data. The fitted parameter values for each specimen are provided in the appendix.

⁴¹⁵ Figure 17 show the resulting retained quasi-elastic modulus as a function of temperature. While values for the retained quasi-elastic modulus of the HS steel foam were widely scattered, the quasi-elastic modulus did not degrade noticeably with increasing temperature (i.e., the value of the retained quasi-elastic modulus was greater than 1.0 across the entire temperature range). The largest increases in retained quasi-elastic modulus were at 200 °C and 300 °C. Conversely, quasi-
⁴²⁰ elastic modulus of Al foam deteriorated rapidly with the increase of the ambient temperature.

5.3.2. Quasi-Hardening Modulus

⁴²⁵ As described above, following yield closed-cell foams exhibit significant plastic hardening, which differs from the elastic-perfectly material behavior where the hardening modulus is assumed to be close to zero. To determine the quasi-hardening modulus, Eq. 11 was fitted using global error minimization techniques to the entire experimental stress-strain curve for each specimen (shown in Figure 15).

⁴³⁰ The fitted parameters enable close approximation of the full stress-strain behavior of both HS steel and PM aluminum foams even throughout the densification phase. Table 4, located in the appendix, presents a summary of the fitted parameter values for each individual specimen. Figure 18 shows the resulting values of the quasi-hardening modulus as a function of temperature.

5.3.3. Densification Strain

⁴³⁵ The point of intersection of the two piecewise curves in Eq. 11 identically defines the inflection point between those segments. The strain location of this inflection point is designated in this study as the densification strain, or the strain at which the tangent slope of the stress-strain curve begins to increase relative to the hardening modulus thereby indicating densification of the metallic

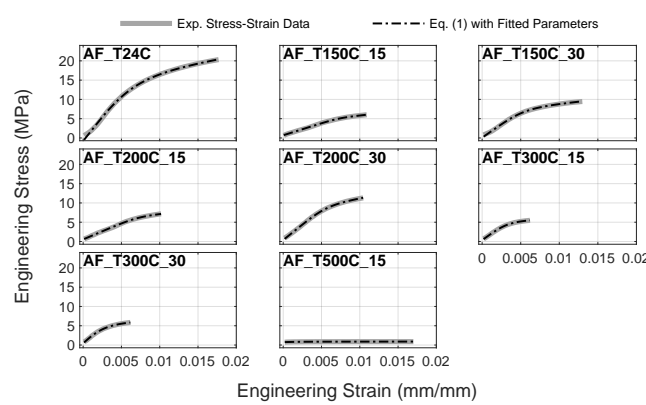
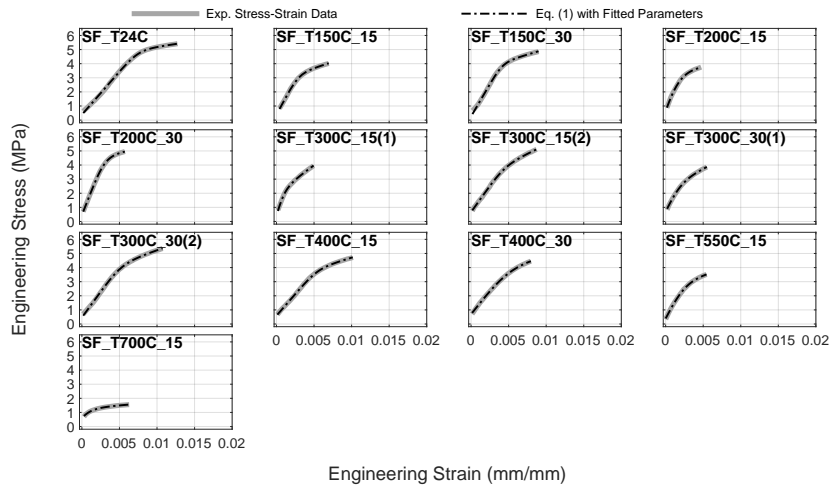


Figure 16: Eq. (9) fitted to the the initial strain range of the stress strain curve for: (a) HS steel foam specimens, and (b) PM aluminum foam specimens. Each plot is denoted by specimen name, using an annotation located in the upper-left-hand corner.

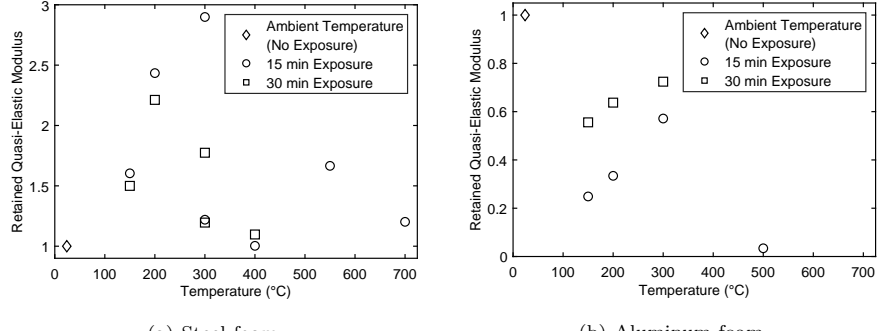


Figure 17: Quasi-elastic modulus.

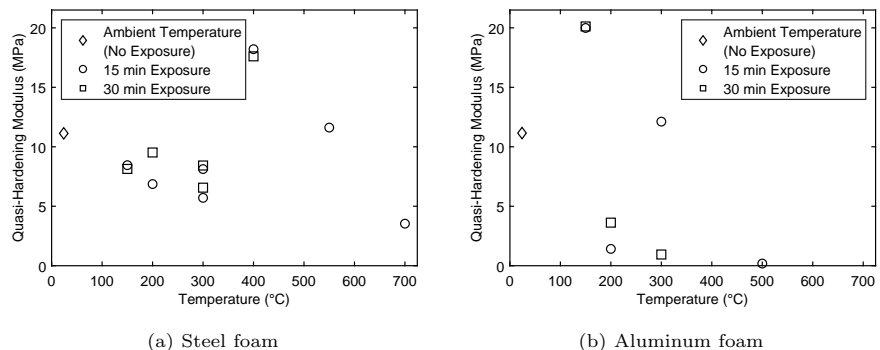


Figure 18: Quasi-hardening modulus did not degrade considerably for steel foam until 700°C , while reduction of Al foam hardening modulus began manifesting itself at 300°C .

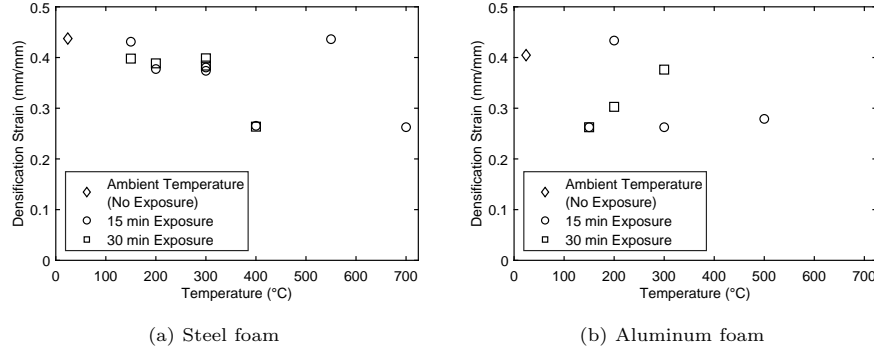


Figure 19: Quasi-hardening modulus did not degrade considerably for steel foam until 700 °C, while reduction of Al foam hardening modulus began manifesting itself at 300 °C.

foam . Figure 19 does not show a clear influence of neither elevated temperatures
⁴⁴⁰ nor exposure on the densification strain. Overall for both the HS steel and PM aluminum foams, the densification strain is scattered by approximately 0.08 mm/mm about a mean densification strain value of about 0.35 mm/mm.

5.3.4. Energy Absorption Efficiency

While ISO Standard 13314:2011 does specify a methodology for calculating
⁴⁴⁵ the energy absorption efficiency, this methodology first requires characterization of the densification strain which could only be reliably determined using the multi-parameter optimization approach described above. The energy absorption efficiency is calculated per ISO Standard 13314:2011 as the ratio of energy absorption capacity to the product of the maximum compressive stress
⁴⁵⁰ (within the strain range spanning from 0.00 mm/mm to the densification strain), and the value of the densification strain (see Figure 20). The energy absorption capacity is shown as the hatched area in Figure 20, and the product of the maximum compressive stress within the strain range and the densification strain is the area bounded by the blue rectangle.

⁴⁵⁵ The energy absorption capacity is calculated either by integrating the stress-strain curve between strains of 0.00 and 0.50, or by multiplying the plateau stress by 1.3. The integration-based approach was used in this study. As expected,

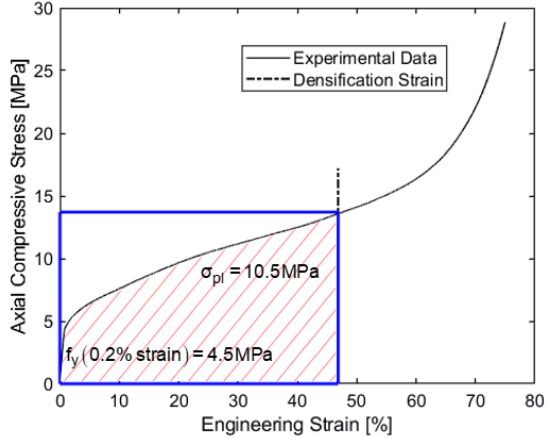


Figure 20: Schematic representation of methodology for calculating energy absorption efficiency.

trends in the behavior of the energy absorption capacity are similar to those of the plateau stress. Interesting, while the energy absorption capacity degrades more quickly with increasing temperature for the PM aluminum foam than for the HS steel foam, the energy absorption capacity of the two types of metallic foams is similar between temperatures of 150 °C and 300 °C (Figure 21). The exposure had relatively little influence on the energy absorption capacity for the HS steel foam; the energy absorption capacity for the two exposures did not differ by more than 4.0 %. The energy absorption capacity of the PM aluminum foam was more scattered, but no systematic influence of exposure on the energy absorption capacity was observed.

For the HS steel foam specimens, the energy absorption efficiency is nearly constant across all tested temperatures at a value of approximately 78 %, and irrespective of the exposure (Figure 22). This trend implies that the shapes of the stress-strain curves are self-similar (at least up to the densification strain) and could be reproduced (in an approximate sense) by scaling the ambient temperature stress-strain response by a temperature dependent scalar reduction factor. Conversely, Aluminum foam exhibited hardening modulus approaching zero at higher temperatures and elastic perfectly plastic behavior with higher

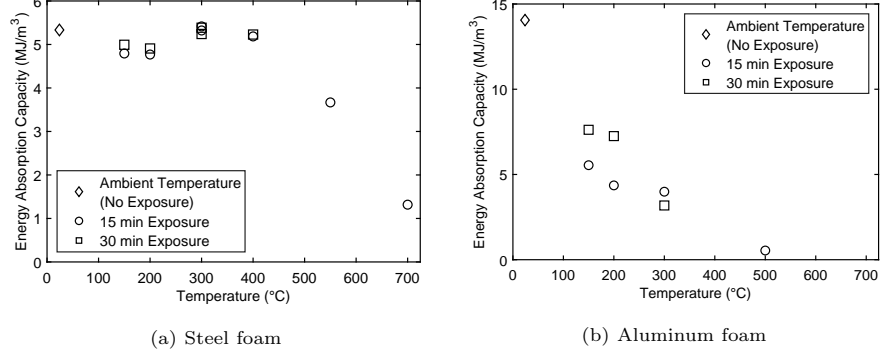


Figure 21: Energy absorption began degrading at 500 °C for steel foam, while reduction for Al foam began manifesting itself at 150 °C.

energy absorption efficiency.

6. Discussion

The computational analyses revealed that the local capacity at the spherical shell level, following initial elastic deformations, was controlled by the plastic buckling and mutual indentation and bending of the spherical shells in contact. These contact regions are distributed randomly throughout the sample and result in localized plasticity. The deformation of the spheres is driven by bending of a spherical region, which increases radially as the material globally hardens. Our computational observations are consistent with a previous study by Fallet et al. [27], who analyzed CT-images from compressive experiments. Fallet proposed using the Weibull distribution to estimate the expected number of contact regions as a function of the overall global strain. Further work is needed to enable analytical predictions of the macroscopic foam properties from the geometry of the hollow spheres and their base material properties through the use of statistics and elasto-plastic analytical modeling of the capacity of a spherical shell. Nevertheless, our computational work indicated that global deterioration of the mechanical capacity of HS foams is controlled by the yield stress of the base metal. In the same time, we have also identified the potential for ultra-thin-walled cellular or tubular structures, which can buckle in the

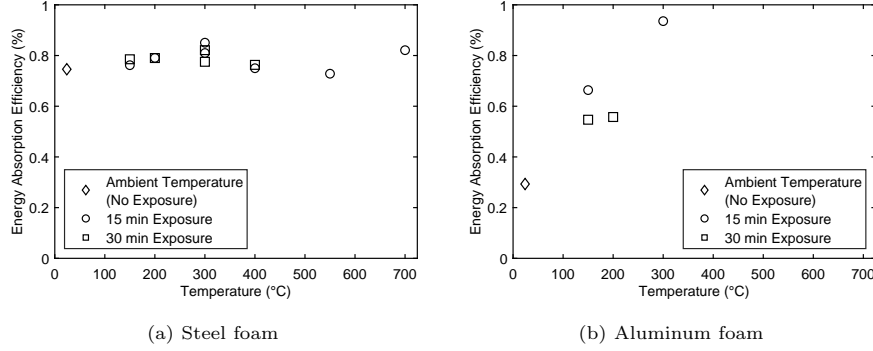


Figure 22: Energy absorption efficiency, calculated per ISO Standard 13314-2011 as the ratio of energy absorption capacity to the product of the maximum compressive stress (within the strain range spanning from 0.00 mm/mm to the densification strain). Energy absorption efficiency was constant for the steel foam, indicating that the thermal deterioration produced self-similar stress-strain curves. On the other hand, Aluminum foam showed increasing trend of the energy absorption efficiency, suggesting that while yield stress dropped sharply, the hardening modulus approached zero, and the material reached an almost elastic-perfectly plastic behavior, with corresponding high energy dissipation efficiency, but lower absolute value.

495 elastic regime. Such materials are expected to exhibit recoverable deformations and their thermal degradation will be controlled by the Young modulus.

As expected based on the fundamental buckling analysis of spherical shells, metallic foam thermal degradations followed the temperature-induced reduction of the plateau stress. We compared Eurocode ([21]), which gives yield stress retention factors of the solid, bulk steel (see Figure 23) to the thermal degradation rate of the hollow sphere steel foam. The data for the HS steel foam followed the trends of the base metal with reasonable consistency. Note that Eurocode does not specify a specific time of exposure, but only states that the heating rate stay between 2 °C/min to 50 °C/min. Thus, it refers to the continuous exposure to the given temperatures. The testing conducted in this study did not show a significant influence of thermal exposure time (15 min or 30 min) on the thermal-mechanical properties of either the HS steel or PM aluminum foams.

According to EN 1999-1-2 [34], the mechanical properties of solid aluminum
510 degrade at much lower temperatures than those of solid steel. Taherishargh et al.
[15] previously reported that the reduction in material properties of foams follow
the trend of the solid material. The yield stress of solid aluminum decreases by
about 20 % at 150 °C and about 90 % at 300 °C; the results for the PM aluminum
foam followed a similar trend, but with even more significant reductions in
515 strength (more than 50 % at 150 °C for some specimens, see Figure 23). The
mechanical performance of the PM aluminum foam was essentially negligible at
temperatures exceeding 300 °C. These findings on aluminum foam behavior at
elevated temperatures (compressive strength, energy absorption capacity and
elastic modulus) are consistent with previous studies of aluminum foams in the
520 literature ([12], [13], [14]).

Although manufacturing of steel foam is more expensive than aluminum
foam due to increased energy costs deriving from the higher melting point of
steel, the retained strength and stiffness of HS steel foam under elevated tem-
peratures is clearly superior to PM aluminum foam. Our observation for the
525 HS steel foam is also consistent with the results for PM steel foams reported
by [16]. The Iron (Fe) based HS steel foam showed only minor degradation in
mechanical performance at temperatures less than 400 °C, and retained 60 % of
its compressive strength at 550 °C. Such resilience might allow steel foam com-
ponents to perform their intended functions even under elevated temperatures,
530 by largely retaining the safety factors embedded in typical designs.

The formation of a blue oxide surface skin during heating of HS steel foam
specimens (see Figure 9) increased its stiffness within the temperature range of
200 °C and 300 °C. These findings are consistent with [16], who reported an
increase in compressive yield strength and stiffness for PM steel foams as the
535 environmental temperature increased up to 400 °C and a decrease above that
temperature. Bekoz et al. [16] suggested aging effect (dynamic age-hardening)
as the reason for the increase in mechanical properties up to 400 °C but did
not detect any enhancement in the compressive strength over the temperature
range.

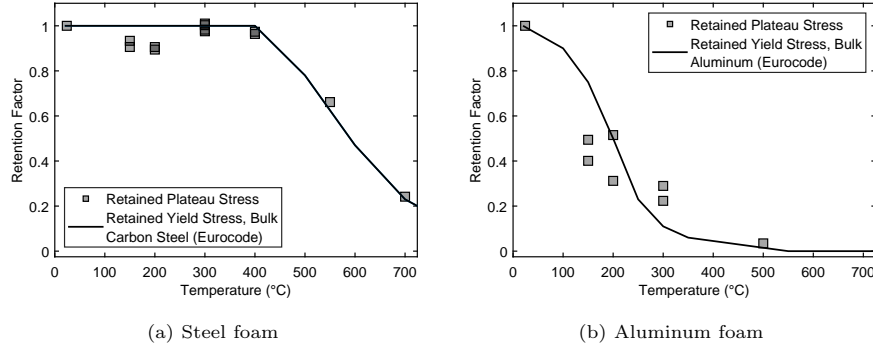


Figure 23: Energy absorption efficiency, calculated per ISO Standard 13314-2011 as the ratio of energy absorption capacity to the product of the maximum compressive stress (within the strain range spanning from 0.00 mm/mm to the densification strain). Energy absorption was constant for the steel foam, indicating that the thermal deterioration produced self-similar stress-strain curves. On the other hand, Aluminum foam showed increasing trend, suggesting that while yield stress dropped sharply, the hardening modulus approached zero, approaching almost elastic-perfectly plastic behavior, with corresponding high energy dissipation efficiency.

540 Considering the large surface areas of metallic foams, surface-oxidizing chemical reactions could have a significant positive influence on the thermal-mechanical performance of steel foams. For example, pre-oxidization of FeCrAl enhances its mechanical properties at temperatures up to 400 °C. The potential for such reactions to reliably increase thermal-mechanical performance should be also investigated for other base metals and alloys because these reactions could allow 545 metallic cellular structures to outperform their constituent base metals.

7. Summary and Conclusions

550 The compressive behavior of hollow sphere (HS) steel foam and powder metallurgy (PM) aluminum foams were studied at elevated temperatures to characterize their thermo-mechanical properties. Compressive loading was applied to each sample, after it had reached a steady-state elevated-temperature of 150 °C, 200 °C, 300 °C, 400 °C, 550 °C or 700 °C for an exposure of 15 min or 30 min. The PM aluminum foam specimens were tested in a similar manner, at temperatures of 150 °C, 200 °C, 300 °C, and 500 °C. Each metallic foam was also tested

555 at ambient temperature (24°C) to obtain its baseline compressive behavior.
Standard metrics for characterizing the temperature-dependent performance of
the metallic foams were calculated based on ISO Standard 13314:2011, and
the behavior was further parametrized by fitting a piecewise nine-parameter
“Richard Equation” to the experimental stress-strain data of each specimen.
560 “Richard equation” parameters for the studied aluminum and steel foams are
listed in the appendix.

The experimental results showed that the HS steel foam retained more than
89 % of its compressive strength, when measured by the plateau stress, up to
400 $^{\circ}\text{C}$. The onset of significant degradation in strength was not until temper-
565 atures beyond 400 $^{\circ}\text{C}$. The HS steel foam retained about 69 % of its strength
and energy absorption capacity at 550 $^{\circ}\text{C}$. At 700 $^{\circ}\text{C}$, much of the structural
integrity of the HS steel foam was largely diminished, retaining only 24 % of
its compressive strength and energy absorption capacity. Contrarily, the PM
aluminum foam began to lose strength and energy absorption capacity immedi-
570 ately with increasing elevated temperatures. The PM aluminum foam retained
only about 45 % of its strength and energy absorption capacity at 150 $^{\circ}\text{C}$, and
had virtually no strength (only 3.5 %) remaining at 500 $^{\circ}\text{C}$.

High-resolution computational analysis of HS steel foam was also performed.
The simulations indicated that the majority of the available metallic foams are
575 controlled by the plastic buckling at local level, which is a function of the ma-
terial yield stress. An observation that was further supported by analytical
consideration of buckling of a spherical shell. Thus, the local plasticity and
plastic stress are critical for the thermal deterioration of metallic foams’ me-
chanical capacities. However, based on the buckling stability considerations, it
580 might be possible to manufacture ultra-thin-walled foams, which should exhibit
highly elastic, reversible deformations. Their thermal behavior is expected to
follow thermal deterioration of Young’s modulus of the base material.

As anticipated from the simulations, the retained plateau stress for both the
HS steel and PM aluminum foams generally followed the elevated-temperature
585 degradation of the yield stress of their respective base metals. The trends for

solid steel and aluminum are available from fire safety standards such as Eurocode EN 1993-1-2:2005 and EN 1999-1-2:2007 for steel and aluminum, respectively.

A blue oxide film, forming on the surface of the steel foam, was highly likely responsible for the moderate increases of quasi-elastic gradient between temperatures of 200 °C and 300 °C and discrepancy between the simulated and experimental stress strain curves of HS foam at 550 °C. Thereby, chemical reactions at elevated temperatures shall be considered in future studies because they could allow metallic foams to exceed thermo-mechanical performance of their base metals by taking advantage of the large surface area to volume ratio in cellular structures.

The high thermal resilience of steel foams suggests that their potential range of application might extend to operations or industrial applications that have traditionally precluded polymeric or even aluminum foams. The energy absorption capacity of the HS steel foam was nearly constant at the temperatures below 400 °C, and significant residual energy absorption capacity (about 69 %) remained at 550 °C. In addition, the energy absorption efficiency was essentially constant at about 80 % and did not diminish at elevated temperatures. Thus, steel foams may be suitable for dissipation of impacts, crashes or other extreme loads at elevated temperatures. It suggests potential applications, where thermal exchange is required at service conditions (e.g. heat sink), and crash absorption is desirable under accidental, extreme load. This research is a part of broader effort to develop understanding of cellular metallic materials with broad relevance to aerospace, automotive, energy and infrastructure applications.

610 List of Symbols

α	Correction factor used for the measurement of the spherical pore size
λ	Slenderness
ν	Poisson ratio

Acronyms

HS	Hollow Sphere
PM	Powder Metallurgy
ISO	International Organization for Standardization
IFAM	Fraunhofer Institute for Manufacturing Technology and Advanced Materials
MTS	Material Testing System
UTM	Universal Testing Machine
RCP	Random close-packed
RT	Room Temperature
SF	Steel Foam
AF	Aluminum Foam
METFOAM	International Conference on Porous Metals and Metallic Foams
EPSRC	Engineering and Physical Science Council

ω_{apex}	Deformation of the sphere apex under uniform pressure
σ_{cr}	Critical limit of membrane stress
σ_{cr}^{shell}	Critical stress of the spherical shell
σ_d	Densification Stress that define the transition to stiffening behavior
$\sigma_{failure}$	Failure stress
σ_{pl}	Plateau Stress
$\sigma_p(T)$	Projection of densification stress at zero strain
σ_{shell}	Buckling Stress of Spherical Shell
σ_y	Yield stress
σ_y^{shell}	Yield stress of the spherical shell
ε	Compressive strain
ε_d	Densification Strain that define the transition to stiffening behavior

$\varepsilon_d(T)$	Densification stiffness
ε_y	Yield strain calculated using the 0.2% offset method
φ	Polar coordinate, where 0 corresponds to the equator and $\pi/2$ to the apex of the sphere
d_c	Diameter of the contact area between the spheres
$E_b(T)$???
$E_d(T)$	Densification stiffness
E_i	Initial elastic modulus
$E_i(T)$	Initial elastic modulus at high temperature
E_p	Plastic hardening modulus
$E_p(T)$	Plastic hardening modulus at high temperature
f_y	Yield stress calculated using the 0.2 offset method
h_{proj}^i	Height of the random cut plane used for measurement of the spherical pore size
$n_b(T)$	Shape parameter that controls the sharpness of the transition from the plastic stiffness to the densification stiffness at high temperature, Figure 7
n_y	Shape parameter that controls the sharpness of the transition from the elastic stiffness to the plastic stiffness
$n_y(T)$	Shape parameter that controls the sharpness of the transition from the elastic stiffness to the plastic stiffness at high temperature
q_c	Pressure applied to a sphere
r_{proj}^i	Projected Radius used for measuring the size of the spherical pore

r_{true}	True Radius of the spherical pore size
650 E	Young Modulus
q	Applied pressure
R	Sphere radius
T	Temperature
t	Sphere Thickness

655 Acknowledgements

The authors would like to express heartfelt gratitude to our academic colleagues for their feedback and fruitful discussions. We are grateful to Fraunhofer IWU in Chemnitz and Fraunhofer IFAM in Dresden for the ongoing collaboration, and for their help with supplying the metallic foam rectangular prisms for 660 mechanical testing.

This study was funded by the Research Framework of the European Commission under METFOAM Career Integration Grant 631827 with support from program manager Dr. Ing. Antonio Cipollaro. The work was also supported by the impact acceleration grant no EP/P511456/1, provided by the Engineering 665 and Physical Science Council (EPSRC) in the UK. Support of Dr. Sue Angulatta, a local program manager, is genuinely appreciated. Any opinions, findings, and conclusions expressed in this article are those of the author(s) and do not necessarily reflect the views of EPSRC or the European Commission.

Data availability

670 The raw data is available upon request and can be uploaded to Elsevier platform.

References

- [1] S. Mahjoob, V. Kambiz, A synthesis of fluid and thermal transport models for metal foam heat exchangers, International Journal of Heat and Mass Transfer 51 (2008) 3701–3711. doi:10.1016/j.ijheatmasstransfer.675
2007.12.012.
- [2] P. Vadwala, Thermal energy storage in copper foams filled with paraffin wax. MSc Thesis, Mechanical and Industrial Engineering - University of Toronto, Toronto, Canada, 2011.
680
- [3] W. Yuan, Y. Tang, X. Yang, Z. Wan, Porous metal materials for polymer electrolyte membrane fuel cells - a review, Applied Energy 94 (2012) 309–329. doi:10.1016/j.apenergy.2012.01.073.
- [4] B. Smith, S. Szyniszewski, J. Hajjar, B. Schafer, S. Arwade, Steel foam for structures: a review of applications, manufacturing and material properties, Journal of Constructional Steel Research 71 (2012) 1–10. doi:10.1016/j.jcsr.685
2011.10.028.
- [5] J. Banhart, H. Seeliger, Aluminum foam sandwich panels: manufacture, metallurgy and applications, Advance Engineering Materials 10 (2008) 793–802. doi:10.1002/adem.200800091.
690
- [6] L. Gibson, M. Ashby, Cellular solids: structure and properties, 2nd Edition, Cambridge University Press, 1999.
- [7] M. Ashby, Metal foams: a design guide, 1st Edition, Butterworth Heinemann, 2000.
695
- [8] L. Lefebvre, J. Banhart, D. Dunand, Porous metals and metallic foams: current status and recent developments, Advance Engineering Materials 10 (2008) 775–787. doi:10.1002/adem.200800241.
- [9] V. Deshpande, N. Fleck, Isotropic constitutive models for metallic foams, Journal of Mechanics and Physics of Solids 48 (2000) 1253–1283. doi:10.1016/S0022-5096(99)00082-4.
699

- 700 [10] A. Reyes, O. Hopperstad, T. Berstad, A. Hanssen, M. Langseth, Constitutive modeling of aluminum foam including fracture and statistical variation of density, European Journal of Mechanics - A/Solids 22 (2003) 815–835.
[doi:10.1016/j.euromechsol.2003.08.001](https://doi.org/10.1016/j.euromechsol.2003.08.001).
- 705 [11] S. Szyniszewski, B. Smith, J. Hajjar, B. Schafer, S. Arwade, The mechanical properties and modeling of a sintered hollow sphere steel foam, Materials and Design 54 (2014) 1083–1094. [doi:10.1016/j.matdes.2013.08.045](https://doi.org/10.1016/j.matdes.2013.08.045).
- [12] M. Aly, Behavior of closed cell aluminium foams upon compressive testing at elevated temperatures: Experimental results, Materials Letters 61 (2007) 3138–3141. [doi:10.1016/j.matlet.2006.11.046](https://doi.org/10.1016/j.matlet.2006.11.046).
- 710 [13] J. Kováčik, L. Orovčík, J. Jerz, High-temperature compression of closed cell aluminium foams, Kovové Materiály 54 (2016) 429–440. [doi:10.4149/km20166429](https://doi.org/10.4149/km20166429).
- 715 [14] J. Liu, Q. Qu, Y. Liu, R. Li, B. Liu, Compressive properties of al-si-sic composite foams at elevated temperatures, Journal of Alloys and Compounds 676 (2016) 239–244. [doi:10.1016/j.jallcom.2016.03.076](https://doi.org/10.1016/j.jallcom.2016.03.076).
- [15] M. Taherishargh, E. Linul, S. Broxtermann, T. Fiedler, The mechanical properties of expanded perlite-aluminium syntactic foam at elevated temperatures, Journal of Alloys and Compounds 737 (2018) 590–596. [doi:10.1016/j.jallcom.2017.12.083](https://doi.org/10.1016/j.jallcom.2017.12.083).
- 720 [16] N. Bekoz, E. Oktay, High temperature mechanical properties of low alloy steel foams produced by powder metallurgy, Materials and Design 53 (2014) 482–489. [doi:10.1016/j.matdes.2013.07.050](https://doi.org/10.1016/j.matdes.2013.07.050).
- [17] Technical Committee ISO/TC 164. Compression test for porous and cellular metals – ISO 13314:2011.
- 725 [18] M. Cobb, World Wide Guide to Equivalent Irons and Steels, 2nd Edition, ASM International, 1987.

- [19] B. Smith, Material characterization and computational simulation of steel foam for use in structural applications. MSc Thesis, University of Massachusetts Amherst, Amherst, Massachusetts, U.S.A., 2012.
- 730 [20] A. Avallone, T. Baumeister, A. Sadegh, Mark's Standard Handbook for Mechanical Engineers, 11th Edition, McGraw-Hill, 2007.
- [21] European Comittee for Standardization. Eurocode 3: Design of Steel Structures, Part 1-2: General Rules - Structural Fire Design – EN 1993-1-2:2005.
- 735 [22] M. Xiong, J. Liew, Mechanical properties of heat-treated high tensile structural steel at elevated temperatures, *Thin-Walled Structures* 98 (2016) 169–176. doi:[10.1016/j.tws.2015.04.010](https://doi.org/10.1016/j.tws.2015.04.010).
- [23] Z. Gao, X. Yu, H. Zhao, Mechanical behavior of metallic hollow sphere materials: experimental study, *J. Aerospace Eng.* 21 (2008) 206–216. doi:[10.1016/\(ASCE\)0893-1321\(2008\)21:4\(206\)](https://doi.org/10.1016/(ASCE)0893-1321(2008)21:4(206)).
- 740 [24] A. Wouterse, A. Philipse, Geometrical cluster ensemble analysis of random sphere packings, *J. Chem. Phys.* 125 (2006) 194709–194719. doi:[10.1063/1.2390700](https://doi.org/10.1063/1.2390700).
- [25] A. Kansal, S. Torquato, F. Stillinger, Computer generation of dense polydisperse sphere packings, *J. Chem. Phys.* 117 (2002) 8212–8218. doi:[10.1063/1.1511510](https://doi.org/10.1063/1.1511510).
- 745 [26] R. Williams, A. Philipse, Random packings of spheres and spherocylinders simulated by mechanical contraction, *Physical Review E* 67 (2003) 1–9. doi:[10.1103/PhysRevE.67.051301](https://doi.org/10.1103/PhysRevE.67.051301).
- [27] A. Fallet, P. Lhuissier, Y. Bréchet, Mechanical behaviour of metallic hollow spheres foam, *Advanced Engineering Materials* 10 (2008) 858–862. doi:[10.1002/adem.200800094](https://doi.org/10.1002/adem.200800094).
- 750 [28] S. Timoschenko, J. Gere, Theory of Elastic Stability, 2nd Edition, Dover Publications, Inc., 2009.

- [29] G. Winter, Strength of thin steel compression flanges, Transactions of ASCE 2035 (1947).
- [30] T. Schaedler, A. Jacobsen, A. Torrents, A. Sorensen, J. Lian, J. Greer, L. Valdevit, W. Carter, Ultralight metallic microlattices, Science 334 (2011) 962–965. doi:10.1126/science.1211649.
- [31] J. Weigand, R. Peixoto, L. Vieira, J. Main, M. Seif, An empirical component-based model for shear behavior of high-strength bolts at elevated temperatures, Journal of Constructional Steel Research 147 (2018) 87–102. doi:10.1016/j.jcsr.2018.03.034.
- [32] M. Richard, J. Abbot, Versatile elastic-plastic stress-strain formulation, Journal of the Engineering Mechanics 101 (1975) 511–515.
- [33] MathWorks, MATLAB Global Optimization Toolbox User's Guide, Version 3.4.1 (R2016b), The MathWorks, Inc., Natick, Massachusetts, United States, 2016.
- [34] European Committee for Standardization. Eurocode 9: Design of Aluminum Structures, Part 1-2: Structural Fire Design – EN 1999-1-2:2007.

770 Appendix

Fitted Richard Equation Parameters

The Richard Equation parameter values fitted only to elastic phase of each specimen's stress-strain response are presented in Table 3, and the Richard Equation parameter values fitted to each specimen's full stress-strain curve are presented in Table 4.

Table 3: Richard Equation Parameters fitted only to Elastic Phase of Specimen Stress-Strain Curve.

Spec.	$E_i(T)$	$E_p(T)$	$\sigma_y(T)$	$n_y(T)$	$E_b(T)$	$E_d(T)$	$\sigma_p(T)$	$n_d(T)$	$(\varepsilon_d, \sigma_d)$
SF_T24C	611	76.9	4.4	10.01	-	-	-	-	-
SF_T150C_15	979	166.8	2.8	5.59	-	-	-	-	-
SF_T150C_30	916	156.5	3.4	7.71	-	-	-	-	-
SF_T200C_15	1487	3.7	4	2.39	-	-	-	-	-
SF_T200C_30	1351	84.8	4.5	4.98	-	-	-	-	-
SF_T300C_15(1)	1770	381	2	2.79	-	-	-	-	-
SF_T300C_15(2)	745	246.1	2.8	5.9	-	-	-	-	-
SF_T300C_30(1)	1084	238	2.5	3	-	-	-	-	-
SF_T300C_30(2)	730	183.1	3.3	6.19	-	-	-	-	-
SF_T400C_15	613	157.4	3	7.6	-	-	-	-	-
SF_T400C_30	670	58.9	4.4	3.43	-	-	-	-	-
SF_T550C_15	1017	78.8	3.4	2.6	-	-	-	-	-
SF_T700C_15	734	35.9	1.3	2.3	-	-	-	-	-
AF_24C	2514	327.2	15.2	2.62	-	-	-	-	-
AF_T150C_15	625	205.9	3.6	9.12	-	-	-	-	-
AF_T150C_30	1397	204.1	6.9	3.88	-	-	-	-	-
AF_T200C_15	840	166.9	5.5	6.21	-	-	-	-	-
AF_T200C_30	1602	347.4	7.7	4.81	-	-	-	-	-
AF_T300C_15	1437	85.6	5.1	3.5	-	-	-	-	-
AF_T300C_30	1820	48	6.2	2.2	-	-	-	-	-
AF_T500C_15	86	2.2	0.8	9.54	-	-	-	-	-

Table 4: Richard Equation Parameters fitted to Specimen Full Stress-Strain Curve.

Spec.	$E_i(T)$	$E_p(T)$	$\sigma_y(T)$	$n_y(T)$	$E_b(T)$	$E_d(T)$	$\sigma_p(T)$	$n_d(T)$	$(\varepsilon_d, \sigma_d)$
SF_T24C	15697	11.1	11.8	0.35	0.44	18.7	84.6	13.1	9.36
SF_T150C_15	12219	8.5	11.5	0.35	0.43	13.7	54	9.3	3.98
SF_T150C_30	22337	8.1	11.2	0.35	0.4	13.6	50.9	8.2	8.32
SF_T200C_15	15550	6.9	11.8	0.34	0.38	12.3	44.1	6.8	9.14
SF_T200C_30	3841	9.5	8.4	0.6	0.39	16.5	64.8	10.8	15.15
SF_T300C_15(1)	3322	8.1	10.2	0.6	0.38	15.9	43.9	11.7	100.28
SF_T300C_15(2)	1146	5.7	9.8	0.99	0.37	15.9	66.8	12.1	107.82
SF_T300C_30(1)	14081	8.4	13.3	0.35	0.4	17.1	63.3	9.6	20.33
SF_T300C_30(2)	3798	6.6	10.5	0.56	0.38	16.7	66.4	10.9	38.01
SF_T400C_15	2554	18.2	6.3	0.84	0.27	15.1	51.8	12.3	6.61
SF_T400C_30	1252	17.6	6.5	1.17	0.26	14	45.5	9.7	12.37
SF_T550C_15	1191	11.6	4.4	1.83	0.44	25	101.9	8.5	5.5
SF_T700C_15	649	3.5	1.8	1.63	0.26	2.9	12.3	3.1	8.03
AF_24C	2565	11.2	26.1	1.44	0.4	37.2	199.6	29.6	5.77
AF_T150C_15	1195	20	6.7	1.58	0.26	9.2	62.7	13.6	3.81
AF_T150C_30	1393	20.1	9.2	3.65	0.26	39.8	75.8	10	39.83
AF_T200C_15	961	1.4	8.5	3.39	0.43	2.9	43.8	11.3	0.79
AF_T200C_30	1694	3.6	13.7	2.4	0.3	3.6	67.6	15.9	20.5
AF_T300C_15	1666	12.1	5.3	3.93	0.26	5.5	45.9	10.6	4.18
AF_T300C_30	2165	0.9	6	2.68	0.38	3.7	59.4	11.8	1.86
AF_T500C_15	3774	0.2	1	0.78	0.28	0.7	6.8	2.2	1.3